Microchimica Acta (2022) 189:430
https://doi.org/10.1007/s00604-022-05519-8

ORIGINAL PAPER

Construction of efficient electrochemiluminescence resonance energy transfer sensor based on SnO_2/SnS_2QDs-Ru@IRMOF-3 composite for sensitive detection of procalcitonin

Dongmiao Qin[1] · Shuo Meng[1] · Yusheng Wu[1] · Zhi Luo[1] · Biyang Deng[1]

Received: 25 May 2022 / Accepted: 30 September 2022 / Published online: 21 October 2022

Abstract

An efficient electrochemiluminescence resonance energy transfer (ECL-RET) method is proposed which combines the luminescent materials of tris(4,4′-dicarboxylicacid-2,2′-bipyridyl) ruthenium(II) (energy donor) and tin dioxide and tin disulfide quantum dots (SnO_2/SnS_2QDs) (energy acceptor) into the isoreticular metal – organic framework-3 (IRMOF-3) material to form a composite. In this mode, the distance between the energy donor and the acceptor was greatly shortened, reducing the energy loss, and thereby effectively improving RET efficiency and further significantly improving the ECL signal. The obtained composite (SnO_2/SnS_2QDs-Ru@IRMOF-3) was combined with sandwich immunoreaction to construct an ECL immunosensor for the sensitive detection of procalcitonin (PCT). Under the optimized experimental conditions with a working potential of – 1.48 V (vs Ag/AgCl), the proposed PCT biosensor exhibited a linear concentration range of 1×10^{-4}–200 ng mL^{-1}, with a detection limit of 0.029 pg mL^{-1} ($S/N = 3$). The biosensor was used to detect PCT in actual samples. The biosensor has broad application prospects in biological analysis and clinical diagnosis due to its high sensitivity, good selectivity, and good stability.

Keywords Electrochemiluminescence · Metal–organic frameworks · Procalcitonin · Quantum dot · Resonance energy transfer

Introduction

Sepsis is a life-threatening global health problem that is thought to be a systemic inflammatory response caused by infections, especially bacterial infections [1]. Patients having cancer and receiving chemotherapy are at high risk of developing infections and even sepsis [2]. Procalcitonin (PCT) levels can be elevated when people have sepsis, multiple organ failure, or a severe infection with bacteria, fungi, or parasites [3–7]. Sepsis can rapidly lead to organ dysfunction, tissue damage, and death if left untreated. Therefore, an accurate and timely diagnosis of sepsis has important clinical significance and necessity. PCT is a molecule with 116 amino acids and a molecular weight of 13 kDa, which has been recognized as a reliable prognostic and therapeutic indicator of sepsis [8]. Some detection strategies have now been used to detect PCT, such as electrochemistry [9–11], surface plasmon resonance [12], enzyme-linked immunosorbent assay [13], time-resolved digital immunoassay [14], microfluidic technology [15], chemiluminescence immunoassay [16], and lateral flow immunoassay [17]. However, the general detection method has low sensitivity and a narrow linear range, and it is difficult to detect the trace amount of PCT in human serum. Therefore, constructing sensitive and efficient detection methods to detect trace PCT in serum is important. Electrochemiluminescence (ECL) has been widely used in biological and clinical analysis, which combines the advantages of electrochemical analysis and chemiluminescence techniques, such as easy control, low background signal, low cost, simple optical equipment, high sensitivity, and good selectivity [18–20]. An ECL immunosensor is constructed based on ECL and specific antibody–antigen recognition technology, enabling specific and sensitive detection of the target [21]. In recent years, ECL

✉ Biyang Deng
dengby16@163.com

[1] State Key Laboratory for Chemistry and Molecular Engineering of Medicinal Resources, School of Chemistry and Pharmaceutical Sciences, Guangxi Normal University, Guilin 541004, China

sensors have been rapidly developed due to the continuous emergence of ECL luminophore.

ECL resonance energy transfer (ECL-RET) is a novel ECL technology that combines high-sensitivity ECL with efficient RET. It has received extensive attention due to its advantages of no excitation light source, avoidance of scattered light, and low background noise [22, 23]. Once an appropriate energy transfer donor (acceptor) is introduced, the ECL efficiency of the energy acceptor (donor) is significantly enhanced (quenched) by RET [24]. Therefore, a key point of ECL-RET is to find suitable donor/acceptor pairs. So far, many donor/acceptor pairs have been reported for the detection of targets, for instance, $Ru(bpy)_2(phen\text{-}NH_2)$-NCNDs (donor) and MoS_2 nanoflowers (acceptor) [25], graphite phase carbon nitride (g-C_3N_4) (donor) and Au–Ag alloy nanoparticles (acceptor) [26], SnS_2@Pt (donor) and $Ru(bpy)_3^{2+}$/Zn-MOF (donor) and gold nanorods (AuNRs) (acceptor) [27], and so on. Although these approaches made great strides, the RET donor and acceptor in these systems were independent and separated by aptamer chains or antigen–antibodies of a specific length. The longer path between the donor and the acceptor based on aptamer chains or antigenic antibodies might lead to energy loss in the energy transfer process, thus limiting the RET efficiency. Under these circumstances, co-immobilizing donor/acceptor pairs within nanostructures to enhance the ECL signal would be a promising method. This technique can also significantly reduce the electron transfer distance and energy loss and increase the effective collision frequency compared with the separation of the donor and the acceptor. Dispersing donor/acceptor pairs in an aqueous medium or immobilizing them on the electrode would greatly enhance the ECL signal of the system. So far, this strategy has been reported to detect targets, such as Luc-SWCNHs-PdCuNCs-PEI-$Ru(Bpy)_2(Mcbpy)^{2+}$ [donor (Luc)/acceptor ($Ru(Bpy)_2(Mcbpy)^{2+}$ pairs] [28] and g-C_3N_4/Ag nanostructures [donor (g-C_3N_4 nanosheets)/acceptor (Ag nanoparticles) pairs] [29], which greatly enhanced the ECL signal due to the shortening of the electron transfer distance and reducing energy loss during the ECL-RET process. Inspired by this, the energy donor and the luminophore acceptor were assembled into a metal–organic framework (MOF) carrier in this study to form a composite material, which was successfully applied for the detection of the target.

MOFs are an important class of functional porous nanomaterials, which use metal ions as linkers and organic ligands as carriers. MOFs have attracted extensive attention in the fields of energy storage [30], separation [31], catalysis [32], drug delivery [33], and sensing [34] due to their inherent properties, including large surface area, favorable pore structure, high porosity, tunable size, and multiple functions [35, 36]. Furthermore, MOFs have been used as a platform for synthesizing novel hybrid materials with excellent chemical properties and may become potential support materials for loading a large number of luminophores to fabricate ECL sensors. In addition, some MOF materials can also enhance the ECL signal between the luminophore and the reactant. For example, isoreticular metal–organic framework-3 (IRMOF-3) with large surface area, high porosity, free amine groups on its backbone structure and multiple functions not only immobilizes a large number of quantum dots (QDs) but also acts as a co-reaction promoter to enhance the ECL intensity [37]. Semiconductor QDs have attracted huge attention of researchers due to their excellent characteristics, such as stable physicochemical properties, strong anti-interference ability, excellent optical and electrical properties, broad absorption spectrum, easy surface modification, easy film formation, good chemical stability, and biocompatibility. However, when QDs are directly applied to ECL sensors, their ECL efficiency is low. In addition, the reagents are wasted, the cost is increased, and their effective collision frequency is low, further limiting the ECL intensity of QDs. Therefore, certain techniques need to be adopted to enhance the luminescence intensity of QDs. In general, the ECL intensity of QDs can be greatly enhanced by the following three methods: (1) a suitable co-reaction promoter can be introduced to enhance the ECL signal; (2) surface modification of QDs to enhance their luminous intensity; and (3) finding suitable energy donors to realize ECL-RET to enhance the ECL intensity of QDs. Tin dioxide and tin disulfide quantum dots (SnO_2/SnS_2QDs) are environment-friendly QDs with low toxicity and high biocompatibility, which were used as luminescent probes in this study. As the main ECL reagents are widely used in various fields, tris(bipyridine)ruthenium(II) complex has also been used in the research of ECL-RET as donors or acceptors, and further applied to construct ECL biosensors with good performance [38].

In this study, an ideal and efficient ECL-RET method was developed using tris(4,4′-dicarboxylicacid-2,2′-bipyridyl) ruthenium(II) ($Ru(dcbpy)_3^{2+}$) as the donor and SnO_2/SnS_2QDs as the acceptor in the composite. SnO_2/SnS_2QDs were linked to $Ru(dcbpy)_3^{2+}$ by amide bonds, and ECL-RET was realized in the nanostructures (SnO_2/SnS_2QDs-Ru). In addition, a large amount of SnO_2/SnS_2QDs-Ru was loaded onto IRMOF-3 to obtain a composite material (SnO_2/SnS_2QDs-Ru@IRMOF-3) to realize ECL-RET more efficiently. This caused the ECL signal to be greatly enhanced due to significantly reduced electron transfer distance and energy loss during the ECL-RET process. IRMOF-3 not only increases the amount of immobilized SnO_2/SnS_2QDs-Ru but also acts as a co-reaction promoter of potassium persulfate, thereby enhancing the ECL intensity of the designed immunosensor system. In addition, the organic ligand 2–aminoterephthalic acid (2-NH_2-BDC) of IRMOF-3 could also promote the conversion of $S_2O_8^{2-}$ co-reactant to sulfate

anion radical ($SO_4^{\bullet-}$), thereby enhancing the ECL intensity of the SnO_2/SnS_2QDs-Ru@IRMOF-3/$S_2O_8^{2-}$ system. The prepared SnO_2/SnS_2QDs-Ru@IRMOF-3 has good biocompatibility and high specific surface area, which could be used to immobilize the target antibody (Ab2). Meanwhile, based on the sandwich immunoreaction, SnO_2/SnS_2QDs-Ru@IRMOF-3 could also be used to construct ECL immunosensors for detecting PCT. The search for new donor/acceptor pairs and the use of large-scale co-immobilization strategies have improved the efficiency of ECL-RET, accelerating the widespread application of ECL technology. Moreover, the sensitive detection of PCT was of great significance for diagnosing and treating sepsis-related diseases.

Experimental section

Reagents

PCT and PCT antibody, amyloid-β_{42} antigen ($A\beta_{42}$), carcinoembryonic antigen (CEA), and prostate-specific antigen (PSA) were purchased from Beijing Biosynthesis Biotechnology Co., Ltd. (Beijing, China). Al_2O_3 powder, tin tetrachloride pentahydrate ($SnCl_4{\cdot}5H_2O$), thiourea (CH_4N_2S), potassium chloride (KCl), disodium hydrogen phosphate dodecahydrate ($Na_2HPO_4{\cdot}12H_2O$), potassium dihydrogen phosphate (KH_2PO_4), and peroxide potassium sulfate ($K_2S_2O_8$) were purchased from Xilong Chemical Co., Ltd. (Guangdong, China). Tris(4,4′-dicarboxylicacid-2,2′-bipyridyl) ruthenium(II) dichloride, potassium ferricyanide ($K_3[Fe(CN)_6]$), potassium ferrocyanide trihydrate ($K_4Fe(CN)_6{\cdot}3H_2O$), bovine serum albumin (BSA), human serum albumin (HSA), chloroauric acid trihydrate ($HAuCl_4{\cdot}3H_2O$), N-hydroxysuccinimide (NHS), 1-ethyl-3-(3-dimethylaminopropyl) carbodiimide (EDC), ethanol, 2-amino terephthalic acid (2-NH_2-BDC), dimethylformamide (DMF), 5,5-dimethyl-pyrroline N-oxide (DMPO), polyvinylpyrrolidone (PVP), and zinc nitrate hexahydrate ($Zn(NO_3)_2{\cdot}6H_2O$) were purchased from Aladdin Industries (Shanghai, China). The experimental reagents were all of analytical grade, and the water was ultrapure water (18.2 MΩ). Serum samples were provided by the Guilin Fifth People's Hospital and stored in a − 20 °C refrigerator for further use.

Apparatus

ECL responses were recorded by the MPI-B multifunctional, electrochemical analytical system (Xi'an Remex Electronic Science-Tech Co., Ltd., China). The voltage of the photomultiplier tube (PMT) was set to 800 V. A three-electrode system composed of platinum wire counter electrode, Ag/AgCl (saturated KCl solution) reference electrode, and glassy carbon electrode (GCE, 3 mm in diameter) was used to perform the ECL experiments. CHI660E A15312 electrochemical workstation (CH Instrument Co., Shanghai, China) was used to study electrochemical impedance spectroscopy. Transmission electron microscopy (TEM) of the synthesized materials was characterized by a Tecnai G2 F20 S-TWIN instrument (FEI, USA) under 200 kV. The surface functional groups of the synthesized materials were characterized by a Fourier transform infrared spectrophotometer (FTIR; Perkin-Elmer, USA). Ultraviolet–visible (UV–vis) absorption spectra were obtained with a Cary 60 UV–vis spectrophotometer (Agilent Technologies, USA). X-ray photoelectron spectroscopy (XPS) of the synthesized materials was characterized using an ESCALAB 250 photoelectron spectrometer (Thermo Fisher Scientific, USA). The X-ray diffraction (XRD) analyses of the material were analyzed by a D/max-2500 V/PC powder X-ray diffractometer (Rigaku, Tokyo, Japan). An electron paramagnetic resonance (EPR) spectrometer was recorded on a Bruker EMX 10/12 spectrometer (Bruker BioSpin GmbH, Rheinstetten, Germany). An FL3-P-TCSPC time-resolved fluorescence spectrometer (Horiba Jobin Yvon, Longjumeau, France) was used to study the fluorescence lifetime of the material. The surface morphology of the prepared materials was characterized using a model Vario Micro Cube scanning electron microscope (SEM) (Elementar Company, Germany). Belsorp-max II was used to measure specific surface area and porosity distribution (Mack Company, Tokyo, Japan).

The phosphate buffer solution (PBS 0.1 M, pH 7.4) was prepared with 0.1 M Na_2HPO_4 and 0.1 M KH_2PO_4. Different pH values of PBS could be adjusted by changing different volume ratios of 0.1 M Na_2HPO_4 and 0.1 M KH_2PO_4. The ferricyanide solution [$Fe(CN)_6^{3-/4-}$] was prepared with potassium ferricyanide and potassium ferrocyanide.

Preparation of SnO_2/SnS_2QDs

SnO_2/SnS_2QDs were synthesized following a previous study [39] with some modifications. The detailed synthesis process is shown in Supplementary Material.

Preparation of SnO_2/SnS_2QDs-Ru

First, 100 µL of mixed solution containing 40 mM EDC and 10 mM NHS (EDC/NHS 4:1) was added to 400 µL of $Ru(dcbpy)_3^{2+}$ (2 mM) solution. The mixture solution was stirred at room temperature (RT) for 15 min to activate the carboxyl group of the $Ru(dcbpy)_3^{2+}$ surface. Next, 800 µL of SnO_2/SnS_2QDs (2 mg mL^{-1}) solution was mixed with the $Ru(dcbpy)_3^{2+}$ solution and stirred continuously for 1 h at RT. The obtained mixture was centrifuged (10,000 rpm, 20 min) and rinsed with 15 mL of ultrapure water for three times to remove excess $Ru(dcbpy)_3^{2+}$ and SnO_2/SnS_2QDs.

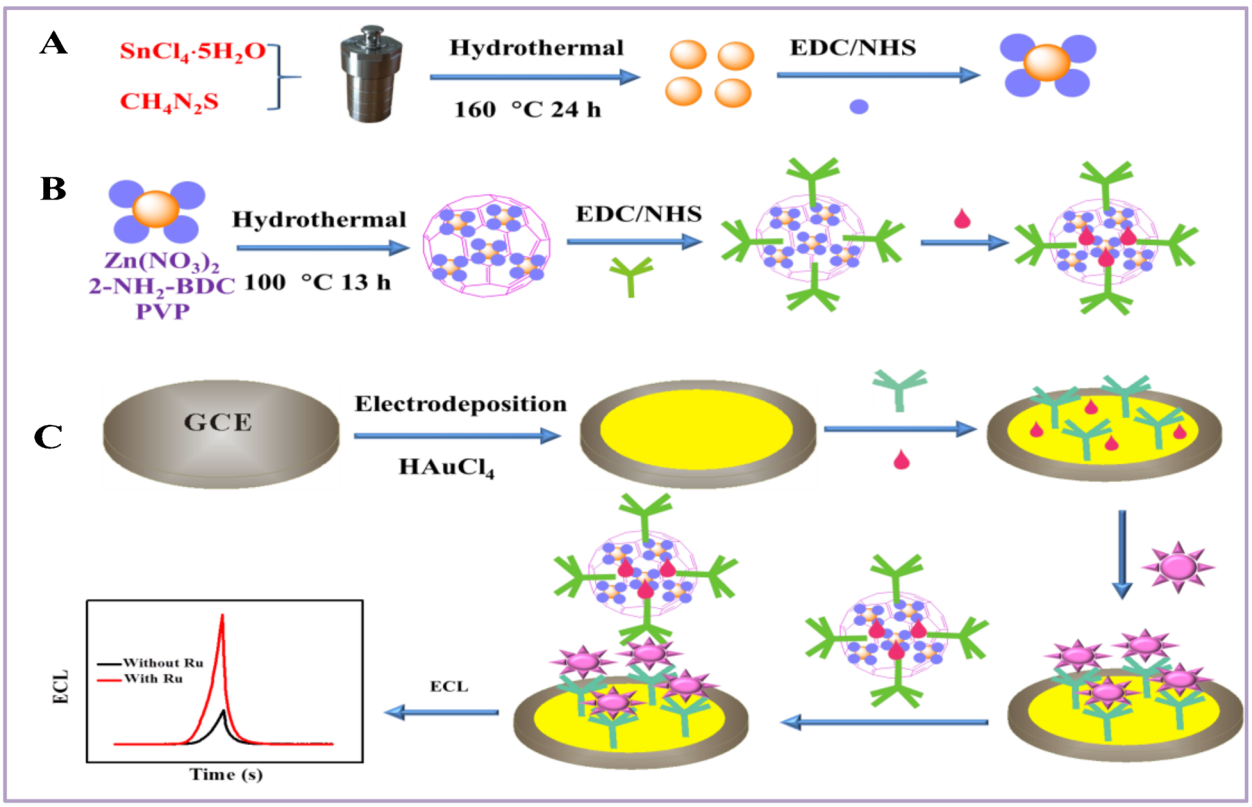
A
$SnCl_4·5H_2O$
CH_4N_2S
Hydrothermal
160 °C 24 h
EDC/NHS
B
$Zn(NO_3)_2$
2-NH_2-BDC
PVP
Hydrothermal
100 °C 13 h
EDC/NHS
C
GCE
Electrodeposition
$HAuCl_4$
ECL
Without Ru
With Ru
Time (s)
ECL

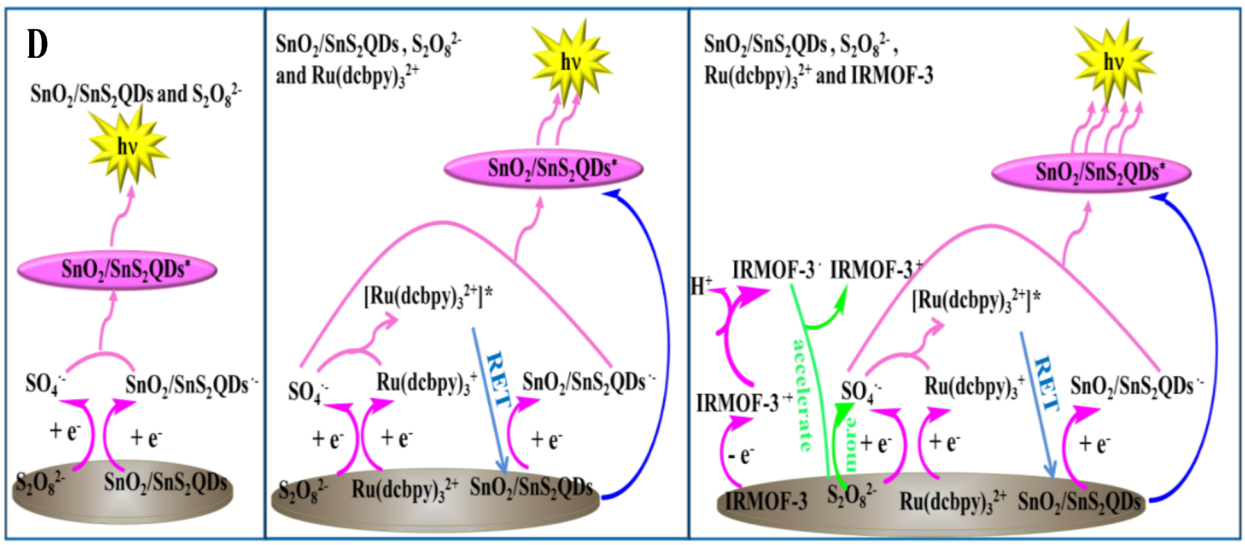
D
SnO_2/SnS_2QDs and $S_2O_8^{2-}$
hν
SnO_2/SnS_2QDs^*
$SO_4^{\cdot-}$
$SnO_2/SnS_2QDs^{\cdot-}$
+ e⁻
+ e⁻
$S_2O_8^{2-}$
SnO_2/SnS_2QDs
SnO_2/SnS_2QDs, $S_2O_8^{2-}$ and $Ru(dcbpy)_3^{2+}$
hν
SnO_2/SnS_2QDs^*
$[Ru(dcbpy)_3^{2+}]^*$
$SO_4^{\cdot-}$
$Ru(dcbpy)_3^{+}$
RET
$SnO_2/SnS_2QDs^{\cdot-}$
+ e⁻
+ e⁻
+ e⁻
$S_2O_8^{2-}$
$Ru(dcbpy)_3^{2+}$
SnO_2/SnS_2QDs
SnO_2/SnS_2QDs, $S_2O_8^{2-}$, $Ru(dcbpy)_3^{2+}$ and IRMOF-3
hν
SnO_2/SnS_2QDs^*
H^+
IRMOF-3$^{\cdot}$
IRMOF-3$^+$
$[Ru(dcbpy)_3^{2+}]^*$
accelerate
more
IRMOF-3$^+$
$SO_4^{\cdot-}$
$Ru(dcbpy)_3^{+}$
RET
$SnO_2/SnS_2QDs^{\cdot-}$
- e⁻
+ e⁻
+ e⁻
+ e⁻
IRMOF-3
$S_2O_8^{2-}$
$Ru(dcbpy)_3^{2+}$
SnO_2/SnS_2QDs

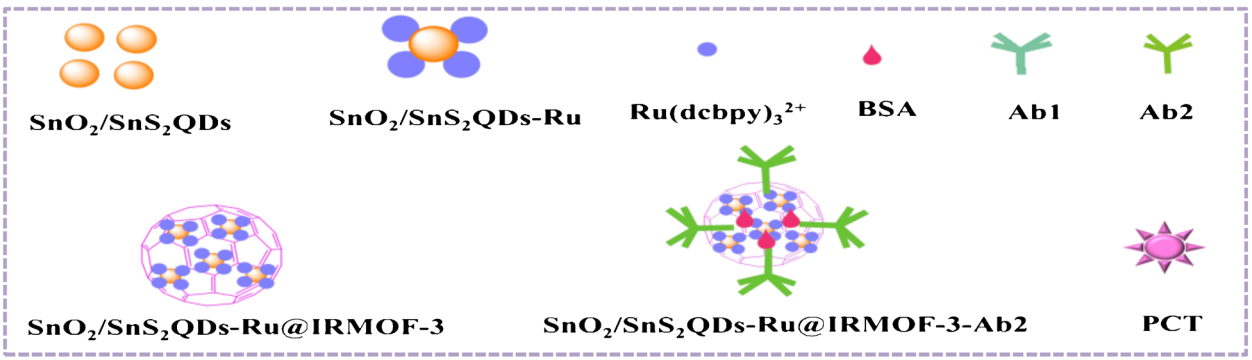
SnO_2/SnS_2QDs
SnO_2/SnS_2QDs-Ru
$Ru(dcbpy)_3^{2+}$
BSA
Ab1
Ab2
SnO_2/SnS_2QDs-Ru@IRMOF-3
SnO_2/SnS_2QDs-Ru@IRMOF-3-Ab2
PCT

◂**Scheme 1** (**A**) Synthesis of SnO_2/SnS_2QDs-Ru composite; (**B**) preparation of SnO_2/SnS_2QDs-Ru@IRMOF-3-Ab2; (**C**) preparation process of ECL immunosensor; and (**D**) ECL-RET and the mechanism of SnO_2/SnS_2QDs-Ru/$S_2O_8^{2-}$ without and with IRMOF-3

In the end, the orange powder product denoted as SnO_2/SnS_2QDs-Ru was obtained by drying at 50 °C and saved in a vacuum drying oven for subsequent use.

Preparation of SnO_2/SnS_2QDs-Ru@IRMOF-3 composite

PVP (0.20 g) was dispersed in a mixed solution containing ethanol (8 mL) and DMF (8 mL). Then, 8 mL of DMF containing 18.1 mg $Zn(NO_3)_2 \cdot 6H_2O$, 4 mg SnO_2/SnS_2QDs-Ru, and 5.4 mg 2-amino terephthalic acid was added to this solution and sonicated for 30 min. Subsequently, the mixture solution was transferred into a 50-mL Teflon-lined autoclave and heated at 100 °C for 5 h. Next, 20 mL of DMF was dissolved in this reaction mixture, and the mixture solution was heated continuously at 100 °C for another 8 h. The reaction produced SnO_2/SnS_2QDs-Ru@IRMOF-3, which was centrifuged (10,000 rpm, 30 min) and washed with ultrapure water (15 mL) for three times. Finally, the obtained product was dried at 50 °C to get an orange powder product SnO_2/SnS_2QDs-Ru@IRMOF-3, which was stored in a vacuum drying oven for further use.

Preparation of SnO_2/SnS_2QDs-Ru@IRMOF-3-Ab2

EDC/NHS (200 µL) mixed solution (40 mM: 10 mM) was added to 1 mL of SnO_2/SnS_2QDs-Ru@IRMOF-3 (2.0 mg mL^{-1}), and then the mixed solution was stirred slowly at RT for 2 h to activate the carboxyl groups on the surface of SnO_2/SnS_2QDs-Ru@IRMOF-3. Next, 200 µL of PCT-Ab2 (10 µg mL^{-1}) was mixed with the SnO_2/SnS_2QDs-Ru@IRMOF-3 solution and stirred continuously at RT for 12 h. Subsequently, to eliminate the nonspecific binding site on the surface of SnO_2/SnS_2QDs-Ru@IRMOF-3, 500 mL of BSA (10 mg mL^{-1}) was added and stirred at RT for 2 h. The obtained precipitate was centrifuged (10,000 rpm, 10 min) and washed with 10 mL of PBS (0.1 M, pH 7.4) two times to unbound excess PCT-Ab2 and BSA. Finally, the obtained SnO_2/SnS_2QDs-Ru@IRMOF-3-Ab2 was dispersed in 2 mL of PBS (0.1 M, pH 7.4) and stored at 4 °C for subsequent experiments.

Preparation of immunosensor

The construction process of the ECL immunosensor is shown in Scheme 1. The treatment process of the bare GCE was referred from a previous study [21]. First, the prepared GCEs were immersed in the $HAuCl_4$ solution (1 wt%) under a constant potential of − 0.2 V and electrochemically deposited for 30 s to obtain a golden yellow thin layer of AuNPs. Next, 8 µL of primary antibody (Ab1, 10 µg mL^{-1}) was coated onto the modified electrode that reacted at 4 °C for 12 h; the captured antibody (Ab1) was immobilized on depAu/GCE via the Au–N affinity. Subsequently, to block nonspecific binding sites, 4 µL of the BSA (10 mg mL^{-1}) solution was added dropwise to the electrode and incubated at RT for 1 h. Next, the modified electrode of BSA/Ab1/depAu/GCE was incubated with 8 µL of a series of PCT antigen concentrations for 1 h at RT. Finally, 8 µL of SnO_2/SnS_2QDs-Ru@IRMOF-3-Ab2 bioconjugate was coated onto the PCT/BSA/Ab1/depAu/GCE and incubated for 1 h at RT to obtain an immune complex. After each modification step, the electrode was gently rinsed with 200 µL of PBS (0.1 M, pH 7.4) to remove the unbound fractions. The obtained sensors were stored at 4 °C when not in use.

Detection conditions of PCT

The ECL cathodic emission was obtained under the following conditions: the detection potential was -1.48 V (vs Ag/AgCl); the PMT voltage was 800 V; the scan rate was 100 mV s^{-1}, and the PBS (0.1 M, pH 7.4) contained 0.1 M $K_2S_2O_8$.

Serum sample preparation

The serum samples were provided by the Guilin Fifth People's Hospital of China and loaded into 5-mL centrifuge tubes. The collected volume of each male serum sample was 1 mL. The serum samples were prepared according to the procedure described in a previous study [40]. Blood was centrifuged at 3500 rpm for 30 min to remove the plasma, and the supernatant serum sample was taken and stored at 4 °C for further analysis.

Results and discussion

Characterization of SnO_2/SnS_2QDs, SnO_2/SnS_2QDs-Ru, and SnO_2/SnS_2QDs-Ru@IRMOF-3 nanocomposites

The TEM was introduced to characterize the morphology and size of the synthesized SnO_2/SnS_2QDs, SnO_2/SnS_2QDs-Ru, and SnO_2/SnS_2QDs-Ru@IRMOF-3. Figure 1 shows the synthesized SnO_2/SnS_2QDs were spherical and aggregate, and the particle size distribution ranged from 1.3 to 5.5 nm with a 3.1 nm average diameter. Figure 1 shows the TEM image of the synthesized SnO_2/SnS_2QDs-Ru. Ru was found to be dispersed on the surface of the synthesized SnO_2/SnS_2QDs. The TEM image of the SnO_2/SnS_2QDs-Ru@

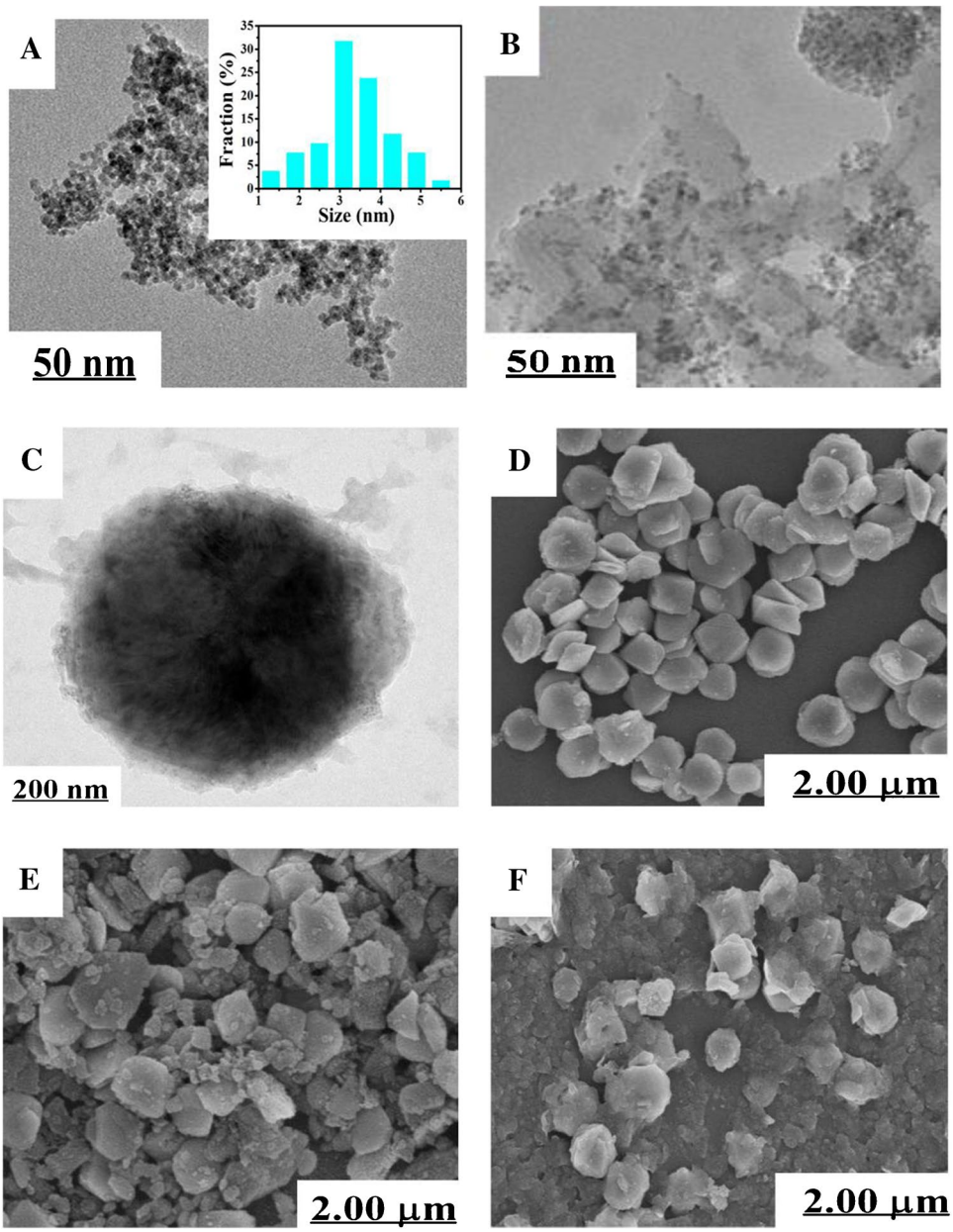

Fig. 1 TEM images of **A** SnO_2/SnS_2QDs (inset: the particle size distribution of SnO_2/SnS_2QDs), **B** SnO_2/SnS_2QDs-Ru, and **C** SnO_2/SnS_2QDs-Ru@IRMOF-3. SEM images of **D** SnO_2/SnS_2QDs, **E** SnO_2/SnS_2QDs-Ru, and **F** SnO_2/SnS_2QDs-Ru@IRMOF-3

IRMOF-3 indicated that the many dots were scattered on the surface of the sphere-like structure (Fig. 1). As shown in Fig. S1, the TEM – energy dispersive X-ray spectroscopy (TEM-EDS) mapping showed the presence of an almost uniform distribution of Ru (Fig. S1A), S (Fig. S1B), Sn (Fig. S1C), O (Fig. S1D), Zn (Fig. S1E), and N (Fig. S1F) elements in SnO_2/SnS_2QDs-Ru@IRMOF-3.

The SEM was used to investigate the morphologies of the synthesized SnO_2/SnS_2QDs, SnO_2/SnS_2QDs-Ru, and SnO_2/SnS_2QDs-Ru@IRMOF-3. Figure 1 shows that the synthesized SnO_2/SnS_2QDs exhibited spherical-like shapes. The SEM image of SnO_2/SnS_2QDs-Ru in Fig. 1 indicates that the surface of SnO_2/SnS_2QDs was scattered with many irregularly shaped Ru. Figure 1 shows that the layered material wrapped SnO_2/SnS_2QDs-Ru, which was caused by the presence of IRMOF-3.

EDS was applied to analyze the elemental compositions of SnO_2/SnS_2QDs, SnO_2/SnS_2QDs-Ru, and SnO_2/SnS_2QDs-Ru@IRMOF-3 composites. Figure 2 shows that the EDS diagram depicted that SnO_2/SnS_2QDs contained five elements, including 0.87% C, 3.12% N, 5.56% O, 30.04% S, and 60.41% Sn. The EDS diagram of SnO_2/SnS_2QDs-Ru is shown in Fig. 2. SnO_2/SnS_2QDs-Ru was found to contain 23.01% C, 8.61% N, 10.53% O, 14.19% S, 31.12% Sn, and 12.54% Ru elements. Figure 2 shows the EDS image of the SnO_2/SnS_2QDs-Ru@IRMOF-3 composite, which contained seven elements: 25.28% C, 3.08% N, 11.56% O, 12.95% S, 27.52% Sn, 8.60% Ru, and 11.01% Zn. XPS was performed

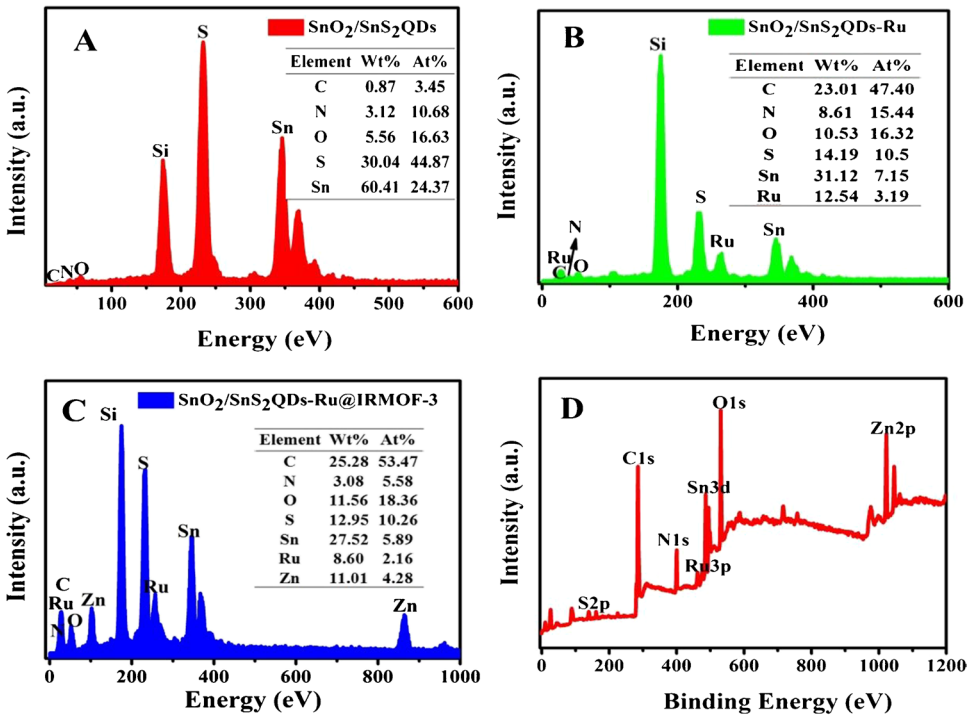

Fig. 2 EDS characterization of **A** SnO_2/SnS_2QDs, **B** SnO_2/SnS_2QDs-Ru, and **C** SnO_2/SnS_2QDs-Ru@IRMOF-3 composites. The XPS full spectrum of **D** SnO_2/SnS_2QDs-Ru@IRMOF-3

to further investigate the chemical states and elementary composition of the synthesized SnO_2/SnS_2QDs-Ru@IRMOF-3. Figure 2 shows that the XPS full spectrum of SnO_2/SnS_2QDs-Ru@IRMOF-3 composite contained seven peaks, namely, S2p, C1s, N1s, Sn3d, Ru3p, O1s, and Zn2p. In addition, the Ru3p region (Fig. S2A), Zn2p region (Fig. S2B), Sn3d region (Fig. S2C), S2p region (Fig. S2D), and O1s region (Fig. S2E) are shown in Supplementary Material (Fig. S2).

The UV–vis spectra of $Ru(dcbpy)_3^{2+}$, IRMOF-3, SnO_2/SnS_2QDs, SnO_2/SnS_2QDs-Ru, and SnO_2/SnS_2QDs-Ru@IRMOF-3 are shown in Fig. S3. The XRD patterns of SnS_2QDs, SnO_2QDs, SnO_2/SnS_2QDs, IRMOF-3, $Ru(dcbpy)_3^{2+}$, SnO_2/SnS_2QDs-Ru, and SnO_2/SnS_2QDs-Ru@IRMOF-3 composite are shown in Figs. S4A and S4B, respectively. The detailed explanations of their UV – vis spectra and XRD patterns are described in Supplementary Material. The FTIR spectra of IRMOF-3, $Ru(dcbpy)_3^{2+}$, SnO_2/SnS_2QDs, SnO_2/SnS_2QDs-Ru, and SnO_2/SnS_2QDs-Ru@IRMOF-3 are shown in Supplementary Material (Fig. S5). The Brunauer – Emmett – Teller (BET) surface area (Fig. S6A) and the pore size distribution curves (Fig. S6B) of IRMOF-3 and SnO_2/SnS_2QDs-Ru@IRMOF-3 were characterized by nitrogen adsorption–desorption isotherms. The detailed explanation is depicted in Supplementary Material.

Mechanism of ECL-RET

The ECL-RET mechanism between $Ru(dcbpy)_3^{2+}$ (energy donor) and SnO_2/SnS_2QDs (energy acceptor) was investigated. A series of filters (wavelengths: 525, 550, 575, 600, 625, 650, 675, 700, and 725 nm) were used to collect the ECL spectra of $Ru(dcbpy)_3^{2+}$, SnO_2/SnS_2QDs, and SnO_2/SnS_2QDs-Ru composites. As shown in Fig. 3, the maximum ECL emission wavelength of $Ru(dcbpy)_3^{2+}$ was located at 625 nm (Fig. 3) and that of SnO_2/SnS_2QDs was located at 675 nm (Fig. 3). Meanwhile, the ECL spectra of the SnO_2/SnS_2QDs-Ru complex alone (Fig. 3, curve a) showed two ECL emission peaks: one with a lower intensity peak corresponding to the emission of $Ru(dcbpy)_3^{2+}$ and the other with a higher intensity peak corresponding to the emission of SnO_2/SnS_2QDs. Curve b was similarly obtained by combining the curves in Fig. 3 and 3; two ECL emission peaks were also observed. The obtained results demonstrated the existence of ECL-RET between SnO_2/SnS_2QDs and $Ru(dcbpy)_3^{2+}$ within one nanostructure, that is, energy transfer from higher bandgap $Ru(dcbpy)_3^{2+}$ to lower bandgap SnO_2/SnS_2QDs was possible. From the obtained experimental data, it was concluded that ECL-RET occurred between $Ru(dcbpy)_3^{2+}$ and SnO_2/SnS_2QDs. Among them, $Ru(dcbpy)_3^{2+}$ acted as an energy donor to emit short wavelengths, while SnO_2/SnS_2QDs acted as an acceptor to emit long wavelengths, resulting in the enhanced ECL intensity of SnO_2/SnS_2QDs.

The ECL-RET mechanism was further demonstrated as follows. The relationship between the ECL spectra of $Ru(dcbpy)_3^{2+}$ and the UV–vis absorption spectra of SnO_2/SnS_2QDs was investigated. As shown in Fig. 4, the maximum ECL emission peak of $Ru(dcbpy)_3^{2+}$ around 625 nm (curve a) and a maximum absorption peak located

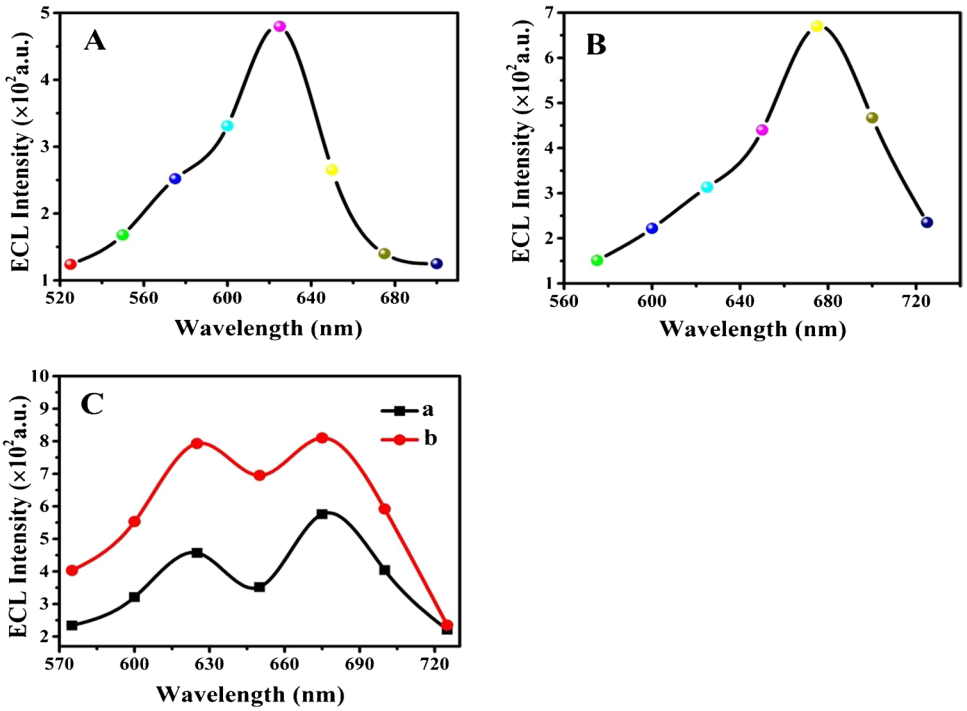

Fig. 3 ECL spectra recorded in PBS (0.1 M, pH 7.4) containing 0.1 M $K_2S_2O_8$: **A** $Ru(dcbpy)_3^{2+}$, **B** SnO_2/SnS_2QDs, and **C** SnO_2/SnS_2QDs-Ru (a), and curve in **A** + curve in **B** (b)

at 485 nm ascribed to SnO_2/SnS_2QDs (curve b) were observed. Further, the UV–vis absorption spectrum of SnO_2/SnS_2QDs overlapped with the ECL emission spectrum of $Ru(dcbpy)_3^{2+}$, proving that ECL-RET might occur between SnO_2/SnS_2QDs and $Ru(dcbpy)_3^{2+}$. The energy transfer efficiency in the donor–acceptor platform could be proved via testing the decay of the donor fluorescence lifetime. Figure 4 shows the fluorescence lifetime curves of $Ru(dcbpy)_3^{2+}$ and $Ru(dcbpy)_3^{2+}$ in the presence of SnO_2/SnS_2QDs. It was observed that the average PL lifetime (τ_{ave}) of $Ru(dcbpy)_3^{2+}$ was 1.07 ns (curve a). When SnO_2/SnS_2QDs were added to $Ru(dcbpy)_3^{2+}$, the average lifetime of $Ru(dcbpy)_3^{2+}$ was weakened to 0.59 ns (curve b). Equation (1) was used to calculate the energy transfer efficiency [41]:

$$E = 1 - (\tau_{da}/\tau_{d}) \quad (1)$$

where τ_{da} and τ_{d} stand for the average PL lifetime of the donor with and without the acceptor, and E represents the energy transfer efficiency. The energy transfer efficiency from $Ru(dcbpy)_3^{2+}$ to SnO_2/SnS_2QDs was counted to be 44.86%, demonstrating the possible energy transfer procedure between $Ru(dcbpy)_3^{2+}$ and SnO_2/SnS_2QDs.

The ECL responses of different modified electrodes were investigated to further clarify the ECL-RET mechanism. The ECL behavior of SnO_2/SnS_2QDs (2 mg mL^{-1}) and SnO_2/SnS_2QDs-Ru (2 mg mL^{-1}) was measured in PBS (0.1 M, pH 7.4, containing 0.1 M $K_2S_2O_8$). As depicted in Fig. 4, the ECL response of SnO_2/SnS_2QDs was about 3595 a.u. (curve a). Compared with the ECL signal of pure SnO_2/SnS_2QDs, the ECL intensity of SnO_2/SnS_2QDs-Ru was significantly increased, and its value was 12,650 a.u. (curve b). In addition, the ECL behavior of SnO_2/SnS_2QDs-Ru (2 mg mL^{-1}) and the pure SnO_2/SnS_2QDs (2 mg mL^{-1}) + pure $Ru(dcbpy)_3^{2+}$ (2 mg mL^{-1}) in the solution was investigated to prove the high efficiency of ECL-RET. Figure 4 shows that the ECL intensity of SnO_2/SnS_2QDs + $Ru(dcbpy)_3^{2+}$ (curve a) was lower than that of SnO_2/SnS_2QDs-Ru composite (curve b). In addition, when SnO_2/SnS_2QDs and $Ru(dcbpy)_3^{2+}$ were controlled in a nanostructure, the ECL peak appeared 0.1 s earlier than SnO_2/SnS_2QDs + $Ru(dcbpy)_3^{2+}$ alone. The results showed that the SnO_2/SnS_2QDs-Ru composite could significantly reduce the energy loss of SnO_2/SnS_2QDs and improve the ECL efficiency of SnO_2/SnS_2QDs due to the short energy transmission path.

ECL mechanism of IRMOF-3 in the SnO_2/SnS_2QDs-Ru/$S_2O_8^{2-}$ system

The ECL behavior of GCE, IRMOF-3/GCE, SnO_2/SnS_2QDs/GCE, $Ru(dcbpy)_3^{2+}$/GCE, SnO_2/SnS_2QDs-Ru/GCE, and SnO_2/SnS_2QDs-Ru@IRMOF-3/GCE was evaluated in 0.1 M PBS (pH 7.4) including $K_2S_2O_8$ (0.1 M) to study the ECL mechanism of IRMOF-3 in the SnO_2/SnS_2QDs-Ru/$S_2O_8^{2-}$ system. Figure 4 shows that the ECL intensity of the bare electrode was extremely weak, and its value was 40 a.u. (curve a); when the IRMOF-3 was added to the GCE surface (curve b), the ECL signal greatly increased to 320 a.u. Further, when detecting SnO_2/SnS_2QDs (curve c) and $Ru(dcbpy)_3^{2+}$ (curve d), it was found that their ECL intensities were 3595 a.u. and 8800 a.u., respectively. Compared

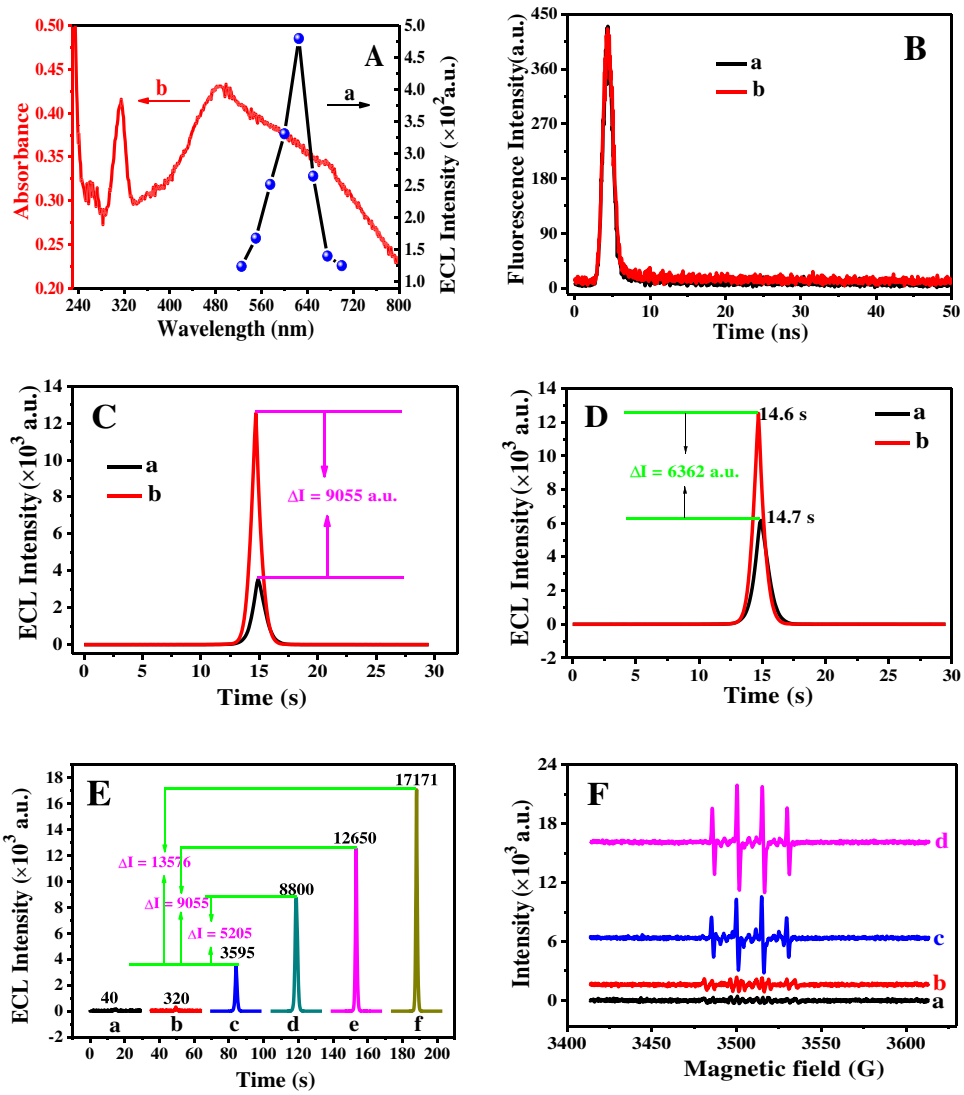

Fig. 4 **A** ECL spectra of $Ru(dcbpy)_3^{2+}$/GCE (curve a) and UV–vis spectra of SnO_2/SnS_2QDs (curve b). **B** Fluorescence lifetime curves of $Ru(dcbpy)_3^{2+}$ without (curve a) and with (curve b) SnO_2/SnS_2QDs. **C** ECL response of SnO_2/SnS_2QDs (curve a) and SnO_2/SnS_2QDs-Ru composites (curve b). **D** ECL signal of pure SnO_2/SnS_2QDs + pure $Ru(dcbpy)_3^{2+}$ (curve a) and SnO_2/SnS_2QDs-Ru composites (curve b). **E** ECL time curves of bare GCE (a), IRMOF-3 (b), SnO_2/SnS_2QDs (c), $Ru(dcbpy)_3^{2+}$ (d), SnO_2/SnS_2QDs-Ru (e), and SnO_2/SnS_2QDs-Ru@IRMOF-3 (f). **F** EPR spectra of (a) PBS and DMPO; (b) IRMOF-3 and DMPO; (c) $S_2O_8^{2-}$ and DMPO; and (d) IRMOF-3, $S_2O_8^{2-}$ and DMPO

with the ECL intensity of pure SnO_2/SnS_2QDs, the ECL response of SnO_2/SnS_2QDs-Ru composite was greatly increased to 12,650 a.u. (curve e) (about 3.5-fold increase), while the ECL signal of SnO_2/SnS_2QDs-Ru@IRMOF-3 significantly increased to 17,171 a.u. (curve f) (about 4.8-fold increase).

The EPR spectroscopy combined with DMPO as the spin-trapping agent was performed to continue investigating the effect of IRMOF-3 on the ECL mechanism of the SnO_2/SnS_2QDs-Ru/$S_2O_8^{2-}$ system. The in situ EPR spectroscopy was used to record for four various solutions: (a) PBS (pH 7.4) and DMPO; (b) IRMOF-3 and DMPO; (c) $S_2O_8^{2-}$ and DMPO; and (d) IRMOF-3, $S_2O_8^{2-}$, and DMPO, where the concentration of PBS, IRMOF-3, and $S_2O_8^{2-}$ was 0.1 M, 2 mg mL^{-1}, and 0.1 M, respectively, and the volume of DMPO was 10 μL. As shown in Fig. 4, the hyperfine cracking constant of the DMPO radical admixture represents the $SO_4^{\bullet-}$ radical added to DMPO ($a_N = 13.2$ G, $a_H = 9.6$ G, $a_H = 1.48$ G, $a_H = 0.78$ G). Furthermore, a representative four-line EPR spectrum with a hyperfine splitting constant was obtained, namely, $a_H = a_N = 14.9$ G, corresponding to DMPO-OH admixture [42]. First, no reaction occurred in PBS (0.1 M, pH 7.4) and DMPO (curve a) or IRMOF-3 and DMPO (curve b) systems, indicating that neither 0.1 M PBS (pH 7.4) nor IRMOF-3 generated $OH^{\bullet}$ or $SO_4^{\bullet-}$. Subsequently, a typical four-line EPR spectrum with a peak ratio of 1:2:2:1 was obtained (curve c), which was attributed to the production of the DMPO-OH adduct. Nevertheless, the response of DMPO-SO_4 was very weak due to the self-sweeping effect of $SO_4^{\bullet-}$ and the reaction between O_2 in the solution and $SO_4^{\bullet-}$ to generate $OH^{\bullet}$ [43]. It showed that when IRMOF-3 was added (curve d), the peak intensities of DMPO-SO_4 and DMPO-OH obviously increased, suggesting that the presence of IRMOF-3 induced the generation of $SO_4^{\bullet-}$ and $OH^{\bullet}$. The reason was the increased reduction

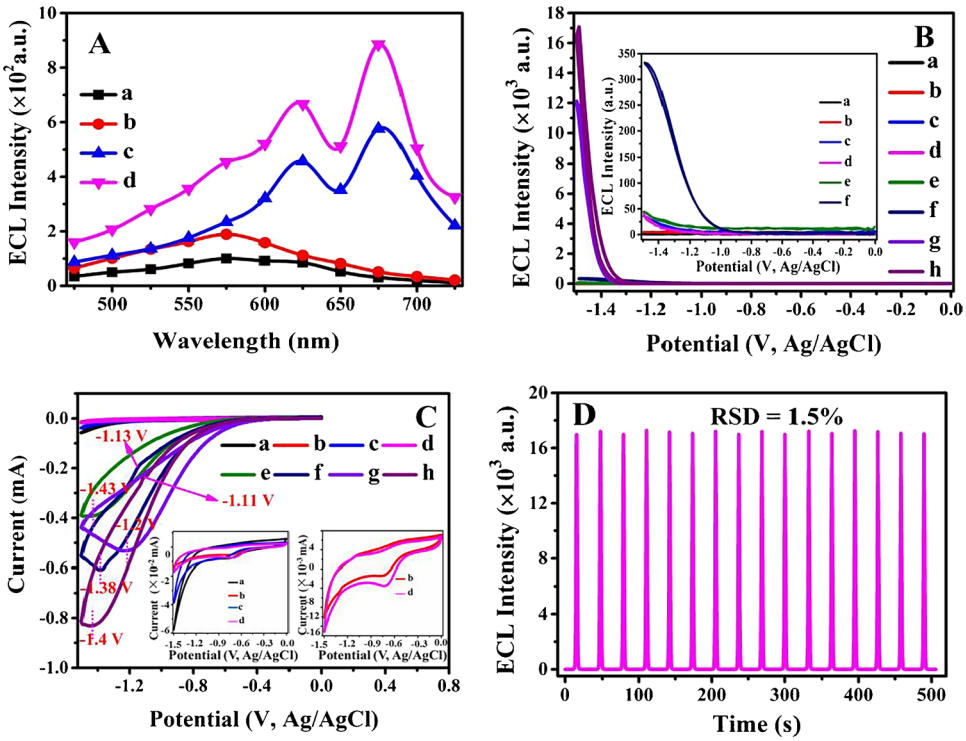

Fig. 5 **A** ECL spectra of (a) bare GCE, (b) IRMOF-3, (c) SnO_2/SnS_2QDs-Ru, and (d) SnO_2/SnS_2QDs-Ru@IRMOF-3. **B** ECL potential curves (inset are enlarged curves of a, b, c, d, e, and f) and **C** CV curves (inset were enlarged curves of a, b, c, and d): (a) PBS, (b) IRMOF-3, (c) SnO_2/SnS_2QDs-Ru, (d) SnO_2/SnS_2QDs-Ru + IRMOF-3, (e) $S_2O_8^{2-}$, (f) IRMOF-3 + $S_2O_8^{2-}$, (g) SnO_2/SnS_2QDs-Ru + $S_2O_8^{2-}$, and (h) SnO_2/SnS_2QDs-Ru + IRMOF-3 + $S_2O_8^{2-}$. **D** ECL signal of the SnO_2/SnS_2QDs-Ru@IRMOF-3 at 16 continuous potential scanning cycles

capacity of $S_2O_8^{2-}$ by IRMOF-3, resulting in the production of more active intermediates as $SO_4^{\bullet-}$.

The ECL spectra of GCE, IRMOF-3, SnO_2/SnS_2QDs-Ru, and SnO_2/SnS_2QDs-Ru@IRMOF-3 were measured in 0.1 M PBS (pH 7.4, containing 0.1 M $K_2S_2O_8$) and were shown in Fig. 5. The maximum emission wavelengths of GCE (curve a) and IRMOF-3 (curve b) were both at 575 nm, which could be attributed to the emission of $1(O_2)_2$* in the $O_2/S_2O_8^{2-}$ system [44]. Besides, the ECL intensity of IRMOF-3 was stronger than that of GCE, indicating that IRMOF-3 might enhance the ECL signal in the $O_2/S_2O_8^{2-}$ system. Curves c and d were the ECL spectra of SnO_2/SnS_2QDs-Ru and SnO_2/SnS_2QDs-Ru@IRMOF-3, respectively. The ECL spectra of SnO_2/SnS_2QDs-Ru and SnO_2/SnS_2QDs-Ru@IRMOF-3 had two ECL signal peaks: the low peak value of 625 nm corresponded to $Ru(dcbpy)_3^{2+}$ and another peak value of 675 nm corresponded to SnO_2/SnS_2QDs. The results indicated that in the SnO_2/SnS_2QDs-Ru@IRMOF-3/$K_2S_2O_8$ system, the SnO_2/SnS_2QDs-Ru was the luminophor and the $K_2S_2O_8$ was the co-reaction. In addition, the ECL intensity of SnO_2/SnS_2QDs-Ru@IRMOF-3 was stronger than that of SnO_2/SnS_2QDs-Ru, indicating that IRMOF-3 acted as a co-reaction promoter of SnO_2/SnS_2QDs-Ru/$K_2S_2O_8$ in the system.

The ECL potential curves and cyclic voltammetry (CV) curves of GCE in eight different solutions [(a) PBS, (b) IRMOF-3, (c) SnO_2/SnS_2QDs-Ru, (d) SnO_2/SnS_2QDs-Ru + IRMOF-3, (e) $S_2O_8^{2-}$, (f) IRMOF-3 + $S_2O_8^{2-}$, (g) SnO_2/SnS_2QDs-Ru + $S_2O_8^{2-}$, and (h) SnO_2/SnS_2QDs-Ru + $S_2O_8^{2-}$ + IRMOF-3] were recorded to evaluate the possible reactions of SnO_2/SnS_2QDs-Ru, $S_2O_8^{2-}$, and IRMOF-3 to further investigate the mechanism of IRMOF-3 in the SnO_2/SnS_2QDs-Ru/$S_2O_8^{2-}$ system. The ECL potential curves are exhibited in Fig. 5. The ECL signal of bare GCE in the PBS (curve a) and IRMOF-3 (curve b) solutions was very weak and could hardly be observed. Curve c was the ECL signal of SnO_2/SnS_2QDs-Ru solution, which was very weak. Curve d was the ECL response of IRMOF-3 + SnO_2/SnS_2QDs-Ru solution, which had little change compared with SnO_2/SnS_2QDs-Ru, indicating that IRMOF-3 had no direct effect on the ECL signal of SnO_2/SnS_2QDs-Ru. In addition, a weak ECL intensity corresponding to the ECL intensity of singlet oxygen [$1(O_2)_2$*] was detected in the $S_2O_8^{2-}$ solution (curve e) [45]. Compared with the $S_2O_8^{2-}$ solution, the ECL intensity of the $S_2O_8^{2-}$ + IRMOF-3 solution (curve f) was increased, the reason might be the reaction of IRMOF-3 with $S_2O_8^{2-}$ to produce the ECL signal. Next, GCE was detected in the solution of SnO_2/SnS_2QDs-Ru + $S_2O_8^{2-}$. Compared with the ECL signal of SnO_2/SnS_2QDs-Ru, its ECL intensity was increased with a value of about 12,650 a.u., indicating that $S_2O_8^{2-}$ was a co-reaction of SnO_2/SnS_2QDs-Ru, which improved the ECL response of the SnO_2/SnS_2QDs-Ru/$S_2O_8^{2-}$ ECL system. Finally, the GCE was detected in the solution of SnO_2/SnS_2QDs-Ru + $S_2O_8^{2-}$ + IRMOF-3 (curve h). Compared with SnO_2/SnS_2QDs-Ru + $S_2O_8^{2-}$, the ECL

intensity significantly increased to 17,171 a.u. According to the experimental results, it was inferred that IRMOF-3 could act as a co-reaction accelerator of SnO_2/SnS_2QDs-Ru/$S_2O_8^{2-}$ in this system to enhance the ECL intensity.

In addition, the CV responses of eight different solutions are shown in Fig. 5. No reduction peak was observed on the bare GCE (curve a). When the GCE was tested in the IRMOF-3 solution (curve b), an oxidation peak was observed at − 1.13 V [46]. Curve c shows that the GCE was measured in the SnO_2/SnS_2QDs-Ru solution, and no redox peak was observed. However, when IRMOF-3 was added to the SnO_2/SnS_2QDs-Ru solution (curve d), an oxidation peak was observed at − 1.13 V. When the GCE was tested in the $S_2O_8^{2-}$ solution (curve e), a significant reduction peak appeared at − 1.43 V due to the strongly reducing intermediate (sulfate anion, $SO_4^{\bullet-}$) formed by electrochemical reduction. Next, the CV behavior of the GCE was evaluated in the solution of $S_2O_8^{2-}$ + IRMOF-3 (curve f), and an oxidation peak was observed at − 1.13 V. In addition, compared with the $S_2O_8^{2-}$ solution, the reduction peak potential was moved positively and the peak current was increased. The results showed that IRMOF-3 could promote the oxidation between SnO_2/SnS_2QDs-Ru and $S_2O_8^{2-}$. Further measurements of the SnO_2/SnS_2QDs-Ru + $S_2O_8^{2-}$ solution (curve g): A reduction potential at − 1.2 V was found and the peak current obviously increased, indicating a strong interaction between SnO_2/SnS_2QDs-Ru and $S_2O_8^{2-}$. Finally, the ECL behavior of the GCE was detected in the solution of SnO_2/SnS_2QDs-Ru + $S_2O_8^{2-}$ + IRMOF-3 (curve h). A reduction potential at − 1.4 V was obtained. Moreover, the peak current dramatically increased compared with the SnO_2/SnS_2QDs-Ru + $S_2O_8^{2-}$. The results showed that IRMOF-3 could accelerate the interaction between SnO_2/SnS_2QDs-Ru and $S_2O_8^{2-}$.

Based on the obtained experimental data and previous studies [43, 46, 47], the possible ECL mechanism of the SnO_2/SnS_2QDs-Ru@IRMOF-3/$S_2O_8^{2-}$ system is shown in Eqs. (2)–(13).

Route:

$$S_2O_8^{2-} + e^- \rightarrow SO_4^{2-} + SO_4^{\bullet-} \quad (2)$$

Route:

$$Ru(dcbpy)_3^{2+} + e^- \rightarrow Ru(dcbpy)_3^{+} \quad (3)$$

$$Ru(dcbpy)_3^{+} + S_2O_8^{2-} \rightarrow Ru(dcbpy)_3^{2+} + SO_4^{\bullet-} + SO_4^{2-} \quad (4)$$

$$Ru(dcbpy)_3^{+} + SO_4^{\bullet-} \rightarrow \left[Ru(dcbpy)_3^{2+}\right]^* + SO_4^{2-} \quad (5)$$

$$\left[Ru(dcbpy)_3^{2+}\right]^* \rightarrow Ru(dcbpy)_3^{2+} + hv(625nm) \quad (6)$$

Route:

$$IRMOF-3 - e^- \rightarrow IRMOF-3^{+\bullet} \quad (7)$$

$$IRMOF-3^{+\bullet} - H^+ \rightarrow IROMOF-3^{\bullet} \quad (8)$$

$$S_2O_8^{2-} + IRMOF-3^{\bullet} \rightarrow IRMOF-3^{+\bullet} + SO_4^{\bullet-} + SO_4^{2-} \quad (9)$$

ECL emission:

$$SnO_2/SnS_2QD_s + e^- \rightarrow SnO_2/SnS_2QD_s^{\bullet-} \quad (10)$$

$$SnO_2/SnS_2QD_s^{\bullet-} + SO_4^{\bullet-} \rightarrow SnO_2/SnS_2QD_s^{*} + SO_4^{2-} \quad (11)$$

$$\left[Ru(dcbpy)_3^{2+}\right]^* + SnO_2/SnS_2QD_s \rightarrow SnO_2/SnS_2QD_s^{*} + Ru(dcbpy)_3^{2+} \quad (12)$$

$$SnO_2/SnS_2QD_s^{*} \rightarrow SnO_2/SnS_2QD_s + hv(675nm) \quad (13)$$

The following three signal amplification strategies were proposed to improve the sensitivity of PCT detection: (1) $Ru(dcbpy)_3^{2+}$ as the energy donor to enhance the ECL intensity of SnO_2/SnS_2QDs; (2) IRMOF-3 as a promoter of co-reactants to enhance ECL signals of luminophor; and (3) IRMOF-3 as a carrier to load more SnO_2/SnS_2QDs-Ru due to its large surface area, thus enhancing the ECL signal. The results indicated that the SnO_2/SnS_2QDs-Ru@IRMOF-3 composite had potential application value in protein analysis. In summary, IRMOF-3 was actually defined as a co-reaction accelerator that interacted with $S_2O_8^{2-}$ rather than SnO_2/SnS_2QDs-Ru and enhanced the ECL signal in the SnO_2/SnS_2QDs-Ru/$S_2O_8^{2-}$ system. The ECL signal of SnO_2/SnS_2QDs-Ru@IRMOF-3/GCE is shown in Fig. 5. The ECL signal was obtained in pH 7.4 PBS (0.1 M) containing 0.1 M $K_2S_2O_8$ under 16 continuous potential scanning cycles. The relative standard deviation (RSD) was 1.5%, indicating excellent stability of SnO_2/SnS_2QDs-Ru@IRMOF-3.

The characterization of immunosensor was recorded via CV (Fig. S7A) and EIS (Fig. S7B), and a detailed explanation is provided in Supplementary Material (Fig. S7). Optimization of the pH (Fig. S8A), $K_2S_2O_8$ concentrations (Fig. S8B), volume ratio of SnO_2/SnS_2QDs with $Ru(dcbpy)_3^{2+}$ (Fig. S8C), $Ru(dcbpy)_3^{2+}$ concentrations (Fig. S8D), SnO_2/SnS_2QDs concentrations (Fig. S8E), and SnO_2/SnS_2QDs-Ru@IRMOF-3 concentrations (Fig. S8F) are shown in Supplementary Material (Fig. S8).

Detection of PCT via the ECL-RET immunosensor

The designed SnO_2/SnS_2QDs-Ru@IRMOF-3 ECL immunosensor was used to detect PCT at optimal conditions. Figure 6 shows that the ECL signal increased gradually with the increase in the PCT concentration (curves a–m). Figure 6 shows a good linear relationship between the ECL signal and the logarithms of PCT concentrations in the range from 1×10^{-4} to

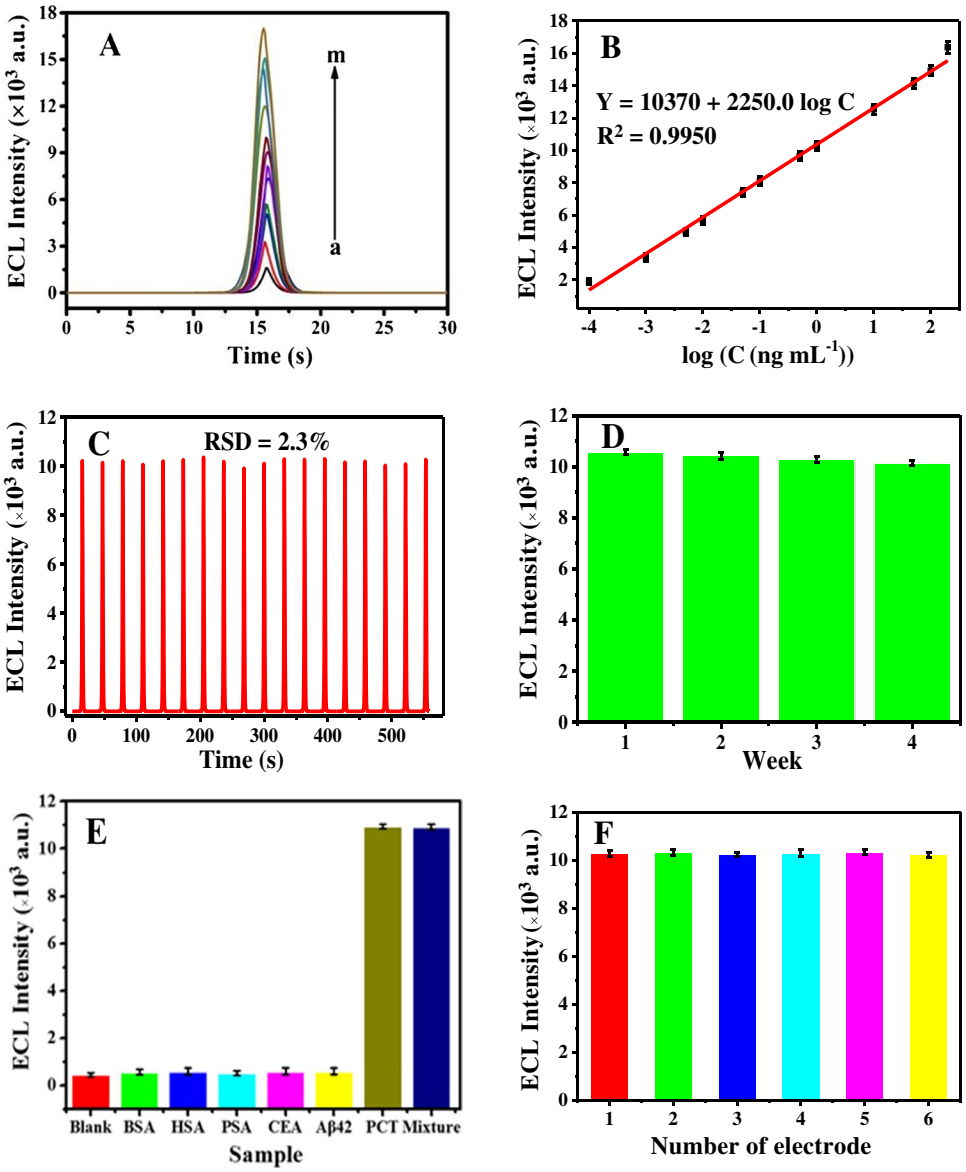

Fig. 6 **A** ECL intensity curves of various PCT concentrations. **B** Linear calibration curve between the logarithm of PCT concentration and ECL intensity. Various PCT concentrations (ng mL^{-1}): (a) 1×10^{-4}, (b) 1×10^{-3}, (c) 5×10^{-3}, (d) 1×10^{-2}, (e) 5×10^{-2}, (f) 0.1, (g) 0.5, (h) 1, (i) 10, (j) 50, (k) 100, and (m) 200. **C** Repeatability of the prepared sensor for 18 cycles. **D** Stability of the sensor after storage for 30 days. **E** Selectivity and specificity of immunosensors: Blank, BSA (10 mg mL^{-1}), HSA (10 mg mL^{-1}), PSA (100 ng mL^{-1}), CEA (100 ng mL^{-1}), $A\beta_{42}$ (100 ng mL^{-1}), PCT (1 ng mL^{-1}), and the mixture. **F** Reproducibility of the proposed ECL immunosensor. (PCT concentration was 1 ng $mL.^{-1}$, $n=3$, error bar = SD). All were measured in 0.1 M PBS (pH 7.4) containing 0.1 M $K_2S_2O_8$

200 ng mL^{-1} ($R^2=0.9950$). Based on the relationship between ECL intensities and log C, the obtained regression equation was $Y=10{,}370+2250.0$ log C (where Y and C represent ECL intensity and PCT concentration, respectively; the unit was ng mL^{-1}). The detection limit was 0.029 pg mL^{-1} ($S/N=3$) for PCT. In addition, the ECL immunosensor designed based on SnO_2/SnS_2QDs-Ru@IRMOF-3 as a luminophor for the detection of PCT had superior ECL performance than other reported detection methods, and the comparison is shown in Table S1. On the contrary, the prepared SnO_2/SnS_2QDs-Ru@IRMOF-3 ECL immunosensor had a lower limit of detection and a wider response range. Therefore, the proposed SnO_2/SnS_2QDs-Ru@IRMOF-3 ECL immunosensor had a potential application prospect in the sensitive detection of PCT.

Stability, selectivity, and repeatability of the immunosensors

Stability was an important factor that affected the performance of immunosensors. Figure 6 shows that the SnO_2/SnS_2QDs-Ru@IRMOF-3 composite did not display significant changes in the ECL signal at 18 continuous potential scanning cycles, and the RSD of ECL intensity was 2.3%. Furthermore, the designed ECL immunosensor was stored at 4 °C for 30 days to investigate its stability, as shown in Fig. 6. The ECL signal of the immunosensor detected by PCT dropped to 5.3% after 30 days. The experimental results showed that the sensor had good stability and a good practical application value.

Table 1 Proposed ECL immunosensor for the determining PCT in human serum ($n = 6$)

Serum sample no	Original (ng mL^{-1})	Added (ng mL^{-1})	Found (ng mL^{-1})	Recovery (%)	RSD (%)	HPRV (ng mL^{-1})
1	0.860	0.800	1.67 ± 0.035	101	2.1	0.88
2	0.0310	0.0500	0.0790 ± 0.0022	96.0	2.8	0.03
3	0.690	0.700	1.37 ± 0.047	97.1	3. 4	0.67

HPRV for hospital-provided reference value

Selectivity was the key characteristic parameter to evaluate the performance of the immunosensor. As shown in Fig. 6, the SnO_2/SnS_2QDs-Ru@IRMOF-3 ECL sensor was incubated with several interfering agents, for example, PSA, CEA, $A\beta_{42}$, BSA, HSA, and the mixture. The ECL intensity displayed no distinct change when compared with the blank control. Furthermore, the ECL intensities were basically uniform when detecting the target object 1 ng mL^{-1} PCT or the mixture. Interference experiments showed that the constructed ECL sensor had a specific response to the sample containing PCT antigen. The results showed that the immunosensor had acceptable selectivity.

The repeatability of immunosensors was also an important standard for the application of immunoassay. Six modified electrodes were prepared to detect 1 ng mL^{-1} PCT under the same experimental conditions to investigate the reproducibility of the proposed ECL sensor. The experimental results are shown in Fig. 6, and the RSD was calculated as 3.5%, indicating that the sensor had satisfactory reproducibility.

Testing of actual samples

The male serum samples were provided by the Guilin Fifth People's Hospital of China. The PCT concentration of the sample was within the linear range of the immunosensor based on the result obtained using the proposed method. Therefore, the samples were not diluted prior to determination. The recovery experiment was used to verify the accuracy of the constructed immunosensor and evaluate the feasibility of its practical application to investigate the feasibility of the immunosensor in clinical application. Three concentrations of PCT (0.800, 0.0500, and 0.700 ng mL^{-1}) were added to the serum samples for a recovery experiment. The experimental results are listed in Table 1. The RSD of PCT in serum samples was as low as 3.4%, and the recoveries were in the range of 96.0–101%, which confirmed the potential application value of the immunosensor in practical sample detection.

Conclusions

In this study, $Ru(dcbpy)_3^{2+}$ could be used as an energy transfer donor, and ECL-RET greatly improved the ECL signal of SnO_2/SnS_2QDs (energy acceptor). The co-immobilization strategy of ECL-RET donor/acceptor pairs coexisting in the same nanocomposite greatly reduced the energy loss and improved the ECL efficiency of SnO_2/SnS_2QDs. An ECL immunosensor was constructed for sensitive detection of PCT. Compared with the previous PCT detection methods, the obtained results had a wide detection range and a low detection limit, indicating that the method had high sensitivity and great potential for the detection of PCT. The prepared immunosensors showed excellent stability, selectivity, and acceptable reproducibility, indicating potential applications in real samples.

Supplementary Information The online version contains supplementary material available at https://doi.org/10.1007/s00604-022-05519-8.

Funding This work was financially supported by the National Natural Science Foundation of China (22164004) and the Guangxi Science Foundation of China (2022GXNSFDA035069).

Declarations

Conflict of interest The authors declare no competing interests.

References

1. Zhang C, Gao J, Wang Z (2018) Bioresponsive nanoparticles targeted to infectious microenvironments for sepsis management. Adv Mater 30:1803618–1803627
2. EI Haddad H, Chaftari A-M, Hachem R, Chaftari P, Raad II (2018) Biomarkers of sepsis and bloodstream infections: the role of procalcitonin and proadrenomedullin with emphasis in patients with cancer. Clin Infect Dis 67:971–977
3. Li H, Sun Y, Elseviers J, Muyldermans S, Liu S, Wan Y (2014) A nanobody-based electrochemiluminescent immunosensor for sensitive detection of human procalcitonin. Analyst 139:3718–3721
4. Feng J, Li F, Liu L, Liu X, Qian Y, Ren X, Wang X, Wei Q (2020) Ultrasensitive photoelectrochemical immunosensor for procalcitonin detection with porous nanoarray $BiVO_4$/Cu_xS platform as

advanced signal amplification under anodic bias. Sensor Actuat B-Chem 308:127685
5. Jia Y, Yang L, Xue J, Ren X, Zhang N, Fan D, Wei Q, Ma H (2019) Highly-branched Cu_2O as well-ordered co-reaction accelerator for amplifying electrochemiluminescence response of gold nanoclusters and procalcitonin analysis based on protein bioactivity maintenance. Biosens Bioelectron 144:111676
6. Xue J, Yang L, Jia Y, Wang H, Zhang N, Ren X, Ma H, Wei Q, Ju H (2019) Electrochemiluminescence double quenching system based on novel emitter $GdPO_4$: Eu with low-excited positive potential for ultrasensitive procalcitonin detection. ACS Sens 4:2825–2831
7. Shao X, Song X, Liu X, Yan L, Liu L, Fan D, Wei Q, Ju H (2021) A dual signal-amplified electrochemiluminescence immunosensor based on core-shell CeO_2-Au@Pt nanosphere for procalcitonin detection. Microchim Acta 188:344
8. Vincenzi B, Fioroni I, Pantano F, Angeletti S, Dicuonzo G, Zoccoli A, Santini D, Tonini G (2016) Procalcitonin as diagnostic marker of infection in solid tumors patients with fever. Sci Rep 6:28090–28095
9. Fang Y, Hu Q, Yu X, Wang L (2018) Ultrasensitive electrochemical immunosensor for procalcitonin with signal enhancement based on zinc nanoparticles functionalized ordered mesoporous carbon-silica nanocomposites. Sensor Actuat B-Chem 258:238–245
10. Ghrera AS (2019) Quantum dot modified interface for electrochemical immunosensing of procalcitonin for the detection of urinary tract infection. Anal Chim Acta 1056:26–33
11. Dutta G, Nagarajan S, Lapidus LJ, Lillehoj PB (2017) Enzyme-free electrochemical immunosensor based on methylene blue and the electro-oxidation of hydrazine on Pt nanoparticles. Biosens Bioelectron 92:372–377
12. Battaglia F, Baldoneschi V, Meucci V, Intorre L, Minunni M, Scarano S (2021) Detection of canine and equine procalcitonin for sepsis diagnosis in veterinary clinic by the development of novel MIP-based SPR biosensors. Talanta 230:122347
13. Rieger M, Kochleus C, Teschner D, Rascher D, Barton AK, Geerlof A, Kremmer E, Schmid M, Hartmann A, Gehlen H (2014) A new ELISA for the quantification of equine procalcitonin in plasma as potential inflammation biomarker in horses. Anal Bioanal Chem 406:5507–5512
14. Jing W, Wang Y, Yang Y, Wang Y, Ma G, Wang S, Tao N (2019) Time-resolved digital immunoassay for rapid and sensitive quantitation of procalcitonin with plasmonic imaging. ACS Nano 13:8609–8617
15. Yang R, Wang J, Gao Y (2019) Advances of microfluidic technologies applied in diagnosis and treatment of sepsis. Zhongguo Wei Zhong Bing Ji Jiu Yi Xue 31:789–792
16. Köszegi T (2002) Immunoluminometric detection of human procalcitonin. J Biochem Biophy Meth 53:157–164
17. Serebrennikova K, Samsonova J, Osipov A (2018) Hierarchical nanogold labels to improve the sensitivity of lateral flow immunoassay. Nano-Micro Lett 10:24–31
18. Qin D, Jiang X, Mo G, Zheng X, Deng B (2020) Electrochemiluminescence immunoassay of human chorionic gonadotropin using silver carbon quantum dots and functionalized polymer nanospheres. Microchim Acta 187:482–494
19. Zhao L, Song X, Ren X, Wang H, Fan D, Wu D, Wei Q (2021) Ultrasensitive near-infrared electrochemiluminescence biosensor derived from Eu-MOF with antenna effect and high efficiency catalysis of specific CoS_2 hollow triple shelled nanoboxes for procalcitonin. Biosens Bioelectron 191:113409–113416
20. Xing B, Zhu W, Zheng X, Zhu Y, Wei Q, Wu D (2018) Electrochemiluminescence immunosensor based on quenching effect of SiO_2@PDA on SnO_2/rGO/Au NPs-luminol for insulin detection. Sensor Actuat B-Chem 265:403–411
21. Qin D, Jiang X, Mo G, Feng J, Yu C, Deng B (2019) A novel carbon quantum dots signal amplification strategy coupled with sandwich electrochemiluminescence immunosensor for the detection of CA15-3 in human serum. ACS Sens 4:504–512
22. Cao J, Liu F, Fu X, Ma J, Ren S, Liu Y (2019) A novel electrochemiluminescence resonance energy transfer system for simultaneous determination of two acute myocardial infarction markers using versatile gold nanorods as energy acceptors. Chem Commun 55:2829–2832
23. Chen Y, Zhou S, Li L, Zhu J (2017) Nanomaterials-based sensitive electrochemiluminescence biosensing. Nano Today 12:98–115
24. Yang L, Fan D, Zhang Y, Ding C, Wu D, Wei Q, Ju H (2019) Ferritin-based electrochemiluminescence nanosurface energy transfer system for procalcitonin detection using HWRGWVC heptapeptide for site-oriented antibody immobilization. Anal Chem 91:7145–7152
25. Bahari D, Babamiri B, Salimi A, Hallaj R, Amininasab SM (2020) A self-enhanced ECL-RET immunosensor for the detection of CA19-9 antigen based on $Ru(bpy)_2(phen\text{-}NH_2)^{2+}$-Amine-rich nitrogen-doped carbon nanodots as probe and graphene oxide grafted hyperbranched aromatic polyamide as platform. Anal Chim Acta 1132:55–65
26. Li P, Ma G, Wu K, Deng A, Li J (2021) An electrochemiluminescence energy resonance transfer system for highly sensitive detection of brombuterol. Talanta 223:121687
27. Mo G, He X, Qin D, Jiang X, Zheng X, Deng B (2021) A potential-resolved electrochemiluminescence resonance energy transfer strategy for the simultaneous detection of neuron-specific enolase and the cytokeratin 19 fragment. Analyst 146:1334–1339
28. Wang H, Liao L, Chai Y, Yuan R (2020) Sensitive immunosensor based on high effective resonance energy transfer of lucigenin to the cathodic electrochemiluminescence of tris(bipyridine) Ru(II) complex. Biosens Bioelectron 150:111915–111919
29. Cao J, Fu X, Zhao L, Ma S, Liu Y (2020) Highly efficient resonance energy transfer in g-C_3N_4-Ag nanostructure: proof-of-concept toward sensitive split-type electrochemiluminescence immunoassay. Sensor Actuat B-Chem 311:127926–127932
30. Makhanya N, Oboirien B, Ren J, Musyoka N, Sciacovelli A (2021) Recent advances on thermal energy storage using metal-organic frameworks (MOFs). J Energy Storage 34:102179–102196
31. Yang H, Wang B, Cheng J, Wang R, Zhang S, Dong S, Wei S, Wang P, Li J (2019) Determination and removal of clenbuterol with a stable fluorescent zirconium (IV)-based metal organic framework. Microchim Acta 186:454–461
32. Yadav S, Dixit R, Sharma S, Dutta S, Solanki K, Sharma RK (2021) Magnetic metal–organic framework composites: structurally advanced catalytic materials for organic transformations. Mater Adv 2:2153–2187
33. Hu J, Chen Y, Zhang H, Chen Z, Ling Y, Yang Y, Liu X, Jia Y, Zhou Y (2021) TEA-assistant synthesis of MOF-74 nanorods for drug delivery and in-vitro magnetic resonance imaging. Microporous Mesoporous Mater 315:110900–110906
34. Mo G, He X, Qin D, Meng S, Wu Y, Deng B (2021) Spatially-resolved dual-potential sandwich electrochemiluminescence immunosensor for the simultaneous determination of carbohydrate antigen 19–9 and carbohydrate antigen 24–2. Biosens Bioelectron 178:113024–113031
35. Li H, Wang X, Zhang X, He M, Zhang J, Liu P, Tang X, Li C, Wang Y (2022) Eu-MOF nanorods functionalized with large heterocyclic ionic liquid for photoelectrochemical immunoassay of a-fetoprotein. Anal Chim Acta 1195:339459
36. Luo Y, Zhao X, Gao Z, Wang H, Liu Y, Guo C, Pan Y (2022) Pd nanoparticles decorated thiol-functionalized MOF as an efficient matrix for differentiation and quantitation of oligosaccharide isomers by laser desorption/ionization mass spectrometry. Anal Chim Acta 1202:339665

37. Yang X, Yu Y, Peng L, Lei Y, Chai Y, Yuan R, Zhuo Y (2018) Strong electrochemiluminescence from MOF accelerator enriched quantum dots for enhanced sensing of Trace cTnI. Anal Chem 90:3995–4002
38. Zhang H, Luo F, Wang P, Guo L, Qiu B, Lin Z (2019) Signal-on electrochemiluminescence aptasensor for bisphenol A based on hybridization chain reaction and electrically heated electrode. Biosens Bioelectron 129:36–41
39. Nathiya D, Gurunathan K, Wilson J (2020) Size controllable, pH triggered reduction of bovine serum albumin and its adsorption behavior with SnO_2/SnS_2 quantum dots for biosensing application. Talanta 210:120671
40. Wu Y, Qin D, Luo Z, Meng S, Mo G, Jiang X, Deng B (2022) High quantum yield boron and nitrogen codoped carbon quantum dots with red/purple emissions for ratiometric fluorescent IO_4^- sensing and cell imaging. ACS Sustainable Chem Eng 10:5195–5202
41. Han Q, Wang C, Li Z, Wu J, Liu P, Mo F, Fu Y (2020) Multifunctional zinc oxide promotes electrochemiluminescence of porphyrin aggregates for ultrasensitive detection of copper ion. Anal Chem 92:3324–3331
42. Wang Y, Liu L, Fang G, Wang L, Kengara FO, Zhu C (2018) The mechanism of 2-chlorobiphenyl oxidative degradation by nanoscale zero-valent iron in the presence of dissolved oxygen. Environ Sci Pollut Res 25:2265–2272
43. Lei Y, Wen R, Zhou J, Chai Y, Yuan R, Zhuo Y (2018) Silver ions as novel coreaction accelerator for remarkably enhanced electrochemiluminescence in a PTCA-$S_2O_8^{2-}$ system and its application in an ultrasensitive assay for mercury ions. Anal Chem 90:6851–6858
44. Lei Y, Zhou J, Chai Y, Zhuo Y, Yuan R (2018) SnS_2 quantum dots as new emitters with strong electrochemiluminescence for ultrasensitive antibody detection. Anal Chem 90:12270–12277
45. Singh D, Baruah JB (2012) Metal(II) complexes derived from conformation flexible cyclic imide tethered carboxylic acids: syntheses, supramolecular structures, and molecular properties. Cryst Growth Des 12:2109–2121
46. Yang F, Yang F, Tu T, Liao N, Chai Y, Yuan R, Zhuo Y (2021) A synergistic promotion strategy remarkably accelerated electrochemiluminescence of SnO_2 QDs for microRNA detection using 3D DNA walker amplification. Biosens Bioelectron 173:112820
47. Ye J, Liu G, Yan M, Zhu Q, Zhu L, Huang J, Yang X (2019) Highly luminescent and self-enhanced electrochemiluminescence of Tris(bipyridine) ruthenium(II) nanohybrid and its sensing application for label-free detection of MicroRNA. Anal Chem 91:13237–13243